Engineering with Computers
https://doi.org/10.1007/s00366-024-02098-5

ORIGINAL ARTICLE

Toward engineering lattice structures with the material point method (MPM)

Oliver Giraldo-Londoño[1] · Rogelio A. Muñetón-López[1] · Paul L. Barclay[2] · Xiatian Zhuang[1] · Duan Z. Zhang[2] · Zhen Chen[1,3]

Received: 29 March 2024 / Accepted: 5 December 2024

Abstract
This study examines the potential of two variants of the material point method—the generalized interpolation material point (GIMP) and dual domain material point (DDMP) methods—in developing a robust computational framework for engineering lattice structures under different loading conditions. The study begins with assessing the ability of the two methods in predicting elastic buckling phenomena using column geometries with and without initial geometric imperfections. The results indicate that both methods effectively capture buckling phenomena when initial geometric imperfections are introduced. After this verification step, we create several models of tetrahedral lattice structures with varying strut diameter and orientation and subject them to quasi-static loading. We then validate the numerical results using laboratory test results. The results show that, while both methods accurately predict load–displacement curves in the pre-buckling regime, their predictive capabilities diminish in the post-buckling regime. Through visual comparison between the numerical and experimental deformed shapes, it appears that the discrepancies between model and experimental results are attributed to initial geometric imperfections in the lattices that occurred during 3D printing. We then establish a second set of lattice models where different types of initial geometric imperfections are considered. The results from these models show that imperfections have a negligible influence in the pre-buckling regime but affect the behavior considerably in the post-buckling regime. As a final step in this work, we subject the lattice models to impact loading and employ hypothetical soft and stiff materials. These results show that the lattice stiffness, which depends on material stiffness, strut diameter, and orientation, significantly influences the ability of a lattice structure to resist impact. In particular, we find that a stiffer lattice (i.e., one made with a stiff material and thicker struts) is capable of absorbing more energy than a softer one during impact. Although material nonlinearities, inelasticity, and detailed contact formulations are not considered in this study, the findings obtained herein lay the groundwork for engineering lattice structures under extreme loading conditions through a simulation-driven framework based on particle-based methods.

Keywords Material point method · GIMP · DDMP · Metamaterials · Lattices · Impact

1 Introduction

The pursuit of innovative materials with enhanced and controlled properties has prompted the development of metamaterials—engineered structures that can achieve properties unattainable by conventional materials. Metamaterials showcase extraordinary capabilities, allowing for tailored designs to achieve specific functionalities, such as superior strength-to-weight ratios or resistance to extreme loading conditions, including high pressures, temperatures, and/or strain rates. One of the main advantages of metamaterials is their ability to be fine-tuned. For instance, properties such as stiffness, strength, or anisotropy can be tailored through lattice structure manipulations, which has

✉ Oliver Giraldo-Londoño
ogiraldo@missouri.edu

✉ Zhen Chen
chenzh@missouri.edu

[1] Department of Civil and Environmental Engineering, University of Missouri, Columbia, MO 65211, USA

[2] Theoretical Division, Fluid Dynamics and Solid Mechanics Group (T-3), Los Alamos National Laboratory, Los Alamos, NM 87545, USA

[3] Department of Mechanical and Aerospace Engineering, University of Missouri, Columbia, MO 65211, USA

Published online: 15 January 2025

motivated their use in a diverse range of energy absorption applications [1–6].

Bioinspiration offers a unique avenue for designing novel metamaterials with unconventional properties. Through billions of years of evolution, some biological materials have developed fascinating hierarchical porous architectures to resist damage. For instance, a recent study revealed a damage-tolerant, dual-scale, single-crystalline microlattice in the biomineralized skeleton of the knobby starfish [7]. The structure of this material is composed of diamond-like tetrahedral unit cells that enhance its damage and failure resistance, thus making it a promising prototype for bioinspired metamaterial design. Inspired by the robust architecture of tetrahedral unit cells found in biological systems, this paper studies the mechanical response of engineered tetrahedral lattice structures under quasi-static loading and explores their potential for impact resistance applications.

Due to the complexity associated with the behavior of lattice structures, robust numerical methods are necessary to predict and optimize their responses. These numerical methods should have the ability to handle responses such as large deformations, self-contact, material nonlinearities, and damage. When attempting to model these responses, mesh-based methods such as the finite element method (FEM) may face challenges and limitations. One such limitation is the need to generate body-fitted meshes with fixed connectivity. Generating such meshes can be time-consuming and prone to numerical instabilities when dealing with large element distortions or failure evolution. While remeshing can alleviate issues associated with large element distortions, this adds implementation complexity and computational expense. In addition to its limitations when modeling very large deformations, Lagrangian finite element formulations may face challenges when modeling buckling phenomena, potentially requiring remeshing or special stabilization techniques.

The limited ability of mesh-based methods to effectively simulate large deformation problems involving multi-phase interactions (e.g., solid–liquid-gas or hard-soft media), and/or failure evolution (e.g., during impact and penetration events) has motivated the development of alternative numerical approaches known as "meshless particle methods" [8]. One of these methods is the material point method (MPM) [9], which uses a Eulerian (fixed) background mesh (grid) to avoid mesh distortion issues and employs a double-mapping between Lagrangian material points (particles) and corresponding grid nodes to better simulate multi-phase interactions.[1] During an MPM integration timestep, the background grid advances with a Lagrangian nodal velocity. However, this Lagrangian nodal velocity is interpolated to the material points before the nodal positions are updated. Because this interpolation occurs before the nodal position update, the grid can be reset, and therefore remaining "static" for the next integration timestep.

Both the FEM and MPM are based on a similar weak formulation of the governing equations, but, unlike FEM, the MPM is a continuum-based particle method that uses particles to represent the material. These particles serve as integration points within the background Eulerian grid. This gives the MPM attributes of both Lagrangian and Eulerian formulations. As shown in several review papers and books [10–14], the MPM has been applied to many areas in simulation-based engineering science, with recent advances being made for improved multi-physics simulation, and high-order accurate and smooth discretization. Moreover, the MPM has found applications in various problems in solid mechanics, including mantle convection [15], silo discharge [16], membrane stretching [17], landfill settlement [18], elastic vibrations [9], collisions [9, 19–21], granular material response [22–25], among others.

While the MPM has proven effective in many applications, its original formulation has been shown to exhibit issues associated with cell-crossing noise, which arise mainly due to the discontinuous gradient of the shape functions [26, 27]. This phenomenon significantly affects the accuracy of the solution, potentially causing premature material failure and alterations in how materials behave during the fracture process [27]. To alleviate this numerical noise, the MPM has been generalized through a variational formulation and a Petrov–Galerkin discretization scheme, leading to the development of the generalized interpolation material point (GIMP) method [28]. The GIMP method improves precision, reduces cell-crossing noise, and expands the capability of the original MPM.

In the GIMP method, tracking the shape of the material points is required [28–30]. However, to avoid this complexity, a modified version of GIMP known as uGIMP simplifies the approach by assuming that the material points have a constant shape, i.e., they do not deform during the deformation process, thereby removing the need for shape tracking. This modification has proven to be effective in scenarios with small deformations [29, 30]. When dealing with problems involving large deformations, however, tracking the shape of the material points remains necessary [28–30]. The dual domain material point (DDMP) method was proposed to overcome this limitation [27]. Unlike the GIMP method, which modifies the shape functions used in the original

[1] For the problems considered in this work, MPM and its advanced versions (GIMP and DDMP) offer no advantage over FEM. Both methods share the same weak formulation, but MPM requires two mapping operations per time step, making it about twice as computationally expensive as FEM in this case. However, this study serves as a first step toward employing MPM to engineering lattice structures under extreme loading involving large deformations and multi-phase interactions.

MPM, the DDMP method only adjusts the gradients of those shape functions. This approach ensures continuity of nodal forces, as material points move across cell boundaries and extends the influence domains of both material points and nodes for gradient-related quantities, while preserving the influence domains for other quantities as related to the original MPM. The DDMP method enhances accuracy in handling large material deformations, thereby providing a robust approach for simulations involving such deformations. Our work employs both the uGIMP and DDMP methods to model the response of tetrahedral lattice structures under quasi-static and dynamic loading, respectively.

Regardless of the method used, unless contact is explicitly modeled, the MPMs will "numerically weld" separate bodies that come close to one another within a single computational cell [23, 25, 31–36]. Bardenhagen et al. [23] proposed a correction step when computing the grid velocity to account for frictionless contact between distinct bodies. This correction step was then expanded to account for frictional contact [35]. Homel and Herbold [31] expanded the contact method to account for self-contact between two distinct parts of the same body. For contact algorithms, accurately computing the surface normal between the bodies is essential for obtaining high-fidelity results [33, 34]. Implementing contact algorithms into our GIMP and DDMP codes is an active area of work, and we plan to study their effects on similar lattice structures in the next phase of our project.

Building on the preceding discussion, this study investigates the features of the GIMP and DDMP methods in developing a robust computational framework tailored to engineering lattice structures under extreme loading conditions. As an initial step towards this overarching goal, the present study uses these two methods to evaluate the quasi-static and dynamic responses of tetrahedral lattice structures. While the proposed framework does not fully account for complex phenomena such as material nonlinearities, inelastic responses, and/or strut-strut frictional contact, this study serves as a pivotal milestone for assessing the suitability of the GIMP and DDMP methods in simulating the large-deformation responses of these lattice structures. By modeling and evaluating various configurations of the lattice structures (e.g., by varying strut thickness and their orientation), our aim is to identify the strengths and limitations inherent in these methods for such applications. The findings from this investigation will lay the groundwork for refining and advancing this computational framework, which will ultimately enable the design of lattice structures for extreme loading applications.

The remainder of the paper is structured as follows. In Sect. 2, we provide the theoretical background and compare the essential features of the GIMP and DDMP methods. Section 3 presents experimental results obtained from quasi-static compression tests conducted on various tetrahedral lattice structures. In Sect. 4, we verify the predictive capabilities of both GIMP and DDMP methods in modeling the buckling response of simplified column models. In Sect. 5, we create GIMP and DDMP models for various tetrahedral lattice structures and compare the numerical results against the experimental results discussed in Sect. 3. Section 6 focuses on investigating the dynamic response of several lattice structures under impact loading using the verified and validated MPM-based codes. Finally, Sect. 7 provides concluding remarks and presents an outlook for future work.

2 Fundamentals of the GIMP and DDMP methods

This section revisits the theoretical foundations of the GIMP and DDMP methods, both derived from the original MPM. As in the FEM, the MPM is based on the weak formulation of the governing equations. Through the double-mapping between material points and corresponding grid nodes, however, the MPM does not employ a fixed mesh connectivity as required in the FEM. The MPM uses shape functions satisfying the Kronecker-delta property, meaning that the shape function $S_i(\boldsymbol{x})$ is nonzero at node i and zero at all other nodes. Within each background cell in the MPM (or element in the FEM), the shape function is often defined as a polynomial in terms of the coordinates in a reference frame. The internal force $\boldsymbol{f}_i^{int}$ at node i is then defined as

$$\boldsymbol{f}_i^{int} = -\int_{\Omega} \boldsymbol{\sigma}(\boldsymbol{x}) \nabla S_i(\boldsymbol{x}) \mathrm{d}V, \tag{1}$$

with Ω being the computational domain.

In the FEM, the integral in Eq. (1) is typically calculated via Gauss integration with the Gauss points being fixed within the corresponding element. In the MPM, this integral is calculated using material points and is approximated as [9]

$$\boldsymbol{f}_i^{int} \approx -\sum\nolimits_p V_p \boldsymbol{\sigma}_p \nabla S_i(\boldsymbol{x}_p), \tag{2}$$

where $\boldsymbol{\sigma}_p$ is the stress at a material point p, $\boldsymbol{x}_p$ is the coordinate of the material point, and $V_p = m_p/\rho_p$ with m_p being the mass associated with the material point and ρ_p being the material density. Owing to its dimensions of volume, V_p is often referred to as the volume of the material point. However, strictly speaking, with this definition of V_p, a material point is essentially a mass point devoid of both shape and volume.

Different from the FEM, the MPM uses a Eulerian (fixed) background cell (grid) for divergence and gradient operations. The Lagrangian capability of the MPM comes from moving material points carrying all the corresponding

information such as mass density, strain, and internal state variables. In other words, the position of the material point, $\boldsymbol{x}_p$, is a function of time. In the original MPM with linear shape functions [9], the shape functions are only required to be continuous, but not smooth across cell boundaries. As a result, when a material point moves across a cell boundary, $\nabla S_i(\boldsymbol{x}_p)$ becomes discontinuous, leading to a discontinuity in the internal force when Eq. (2) is used. This discontinuity often leads to numerical noise and failure of the numerical calculations [28]. Both DDMP and GIMP address this issue by having continuous gradients of the shape functions. Alternatively, higher order B-spline shape functions (i.e., quadratic or cubic) can also be used to address this issue if a structured mesh is used.

The generalized interpolation material point (GIMP) method [28] was developed to address this issue of internal force discontinuity. This is achieved by introducing a particle domain for defining the shape functions. In the GIMP, a material point is no longer a geometric mass point, but a finite domain of the material. In other words, in addition to the discretization of the background grid, the GIMP introduces another discretization by dividing the material into small domains (still called material points). Given that the GIMP considers a material point as a finite domain, as the material deforms and moves in each time step, a portion of the material point may move across cell boundaries. As a result, only the portion of the material point within the cell is considered when calculating the internal force contribution from each material point. Because it takes time for a material point domain to move across a cell boundary completely, the internal force calculated this way becomes continuous, thus eliminating the cell-crossing noise inherent in the original MPM.

These domains of material points are supposed to cover the entire material without overlap. This condition is often termed *partition of unity*, since one can define a characteristic function for each of these domains. When the domains cover the entire material without overlap, the characteristic functions sum to unity everywhere. When this condition is satisfied, the GIMP method satisfies conservation of mass and momentum. For one-dimensional problems, this condition is easy to be satisfied. For two- or three-dimensional problems, however, one could easily create material point domains that satisfy this condition initially but maintaining it throughout the calculation is more challenging, especially for those cases involving large deformations and failure evolution.

One way to avoid the above issue is to relax this restriction and allow for certain errors in satisfying the condition of partition of unity. One such approach is called uGIMP [27], in which the center of the domain associated with a material point moves with the point, but the domain is not allowed to deform in the calculation. In this way, the uGIMP method approximately satisfies partition of unity, but gaps and overlaps between the domains can happen. To improve the uGIMP, another approach called cpGIMP was introduced [27]. In the cpGIMP method, the material point domain can stretch and compress along the directions of the coordinate axes, but it does not account for shear deformation or rotation.

To allow for shear deformations and rotation of the particle domain, convected particle domain interpolation (CPDI) methods [30, 31] have been introduced. In CPDI methods, the local deformation gradient around the material point is used to deform the domain of a material point such that the gaps and overlaps between the domains are reduced, with additional computational expenses as compared with the GIMP methods. To balance computational accuracy and efficiency, we utilize the uGIMP method [27] in this study but refer to it as the GIMP method from here on.

The DDMP method [27] also seeks to address the internal force discontinuity issues discussed earlier, but it employs a different approach. In the DDMP method, material points are still treated as geometric mass points. The stress at a material point is divided into two parts using a partition function $\alpha(\boldsymbol{x}_p)$, which takes a value of zero on cell boundaries. The first part, $\alpha(\boldsymbol{x}_p)\boldsymbol{\sigma}_p$, of the stress is considered in the same way as the MPM, namely by replacing the stress $\boldsymbol{\sigma}_p$ with $\alpha(\boldsymbol{x}_p)\boldsymbol{\sigma}_p$ in Eq. (2). Since $\alpha(\boldsymbol{x}_p) = 0$ on the cell boundary related to any material point, the cell crossing discontinuity is eliminated for this part. The second part, $[1 - \alpha(\boldsymbol{x}_p)]\boldsymbol{\sigma}_p$, of the stress is mapped to the surrounding nodes using the typical particle-to-node mapping in the MPM to obtain a discounted (by α) nodal stress $\boldsymbol{\sigma}_i^d$. This nodal stress can then be interpolated into corresponding cells as

$$\boldsymbol{\sigma}^d(\boldsymbol{x}) = \sum\nolimits_j \boldsymbol{\sigma}_j^d S_j(\boldsymbol{x}). \tag{3}$$

Since the shape function is continuous on the cell boundaries, $\boldsymbol{\sigma}_i^d$ is continuous as the material points move across cell boundaries. This stress is then substituted into Eq. (1) to determine its contribution to the nodal force. Combining both parts of the stress from the material points, the internal force at a corresponding node is then given by

$$\boldsymbol{f}_i^{int} \approx -\sum\nolimits_p V_p \boldsymbol{\sigma}_p \alpha(\boldsymbol{x}_p) \nabla S_i(\boldsymbol{x}_p) - \sum\nolimits_j \boldsymbol{\sigma}_j^d \int_\Omega S_j(\boldsymbol{x}) \nabla S_i(\boldsymbol{x}) \mathrm{d}V. \tag{4}$$

Because $\boldsymbol{\sigma}_i^d$ is continuous and $\alpha(\boldsymbol{x}_p) = 0$ on the cell boundaries, the internal force calculated this way is continuous as material points move across cells. The integral in Eq. (4) is independent of the stresses and locations of material points, and only needs to be calculated once in a calculation. Because of the supports of the shape functions,

this integral is only nonzero if nodes i and j share the same cell.

In principle, the internal force calculated with Eq. (4) depends on $\alpha(\boldsymbol{x}_p)$. In practice, the results are insensitive to the choice of this function, especially for calculations with sufficient mesh resolution, because the internal force from Eq. (4) converges to that from Eq. (1) with the cell refinement [27]. The function $\alpha(\boldsymbol{x}_p)$ is only required to be continuous and positive, with $\alpha(\boldsymbol{x}_p) = 0$ on the cell boundaries. In this study, we adopt the following expression for $\alpha(\boldsymbol{x}_p)$, because it generally yields satisfactory results in many DDMP calculations [27]:

$$\alpha(\boldsymbol{x}_p) = 0.5\left\{\prod_{i=1}^{n_c} 2[S_i(\boldsymbol{x}_p)]\right\}^{\frac{3}{2(n_c-1)d}}, \tag{5}$$

where n_c is the number of nodes for the cell containing $\boldsymbol{x}_p$, and d is the problem dimension.

Since $\boldsymbol{\sigma}_i^d$ is calculated from the stresses at material points, we can define a function $\overline{\nabla S_i}(\boldsymbol{x})$, called modified gradient of the shape function, to rewrite Eq. (4) in terms of the stresses at the material points:

$$\boldsymbol{f}_i^{int} \approx -\sum\nolimits_p V_p \boldsymbol{\sigma}_p \overline{\nabla S_i}(\boldsymbol{x}_p), \tag{6}$$

where

$$\overline{\nabla S_i}(\boldsymbol{x}) = \alpha(\boldsymbol{x})\nabla S_i(\boldsymbol{x}) + [1-\alpha(\boldsymbol{x})]\sum\nolimits_j^n \frac{S_j(\boldsymbol{x})}{V_j}\int_\Omega S_j(\boldsymbol{x})\nabla S_i(\boldsymbol{x})\mathrm{d}V, \tag{7}$$

with V_j being the volume associated with node j. In this way, the DDMP method can be regarded as a version of the MPM that uses the original shape functions, but with the gradient of the shape functions being modified as shown in Eq. (7). The material points in the DDMP method remain to be geometrical mass points, and hence, there is no need to track the shape change in the calculation.

Since the original shape function satisfies the partition of unity, mass conservation is guaranteed in the DDMP method. One can also show that the modified shape function gradient satisfies the following [27]:

$$\sum\nolimits_i \overline{\nabla S_i}(\boldsymbol{x}_p) = 0, \sum\nolimits_i \boldsymbol{x}_i \overline{\nabla S_i}(\boldsymbol{x}_p) = I. \tag{8}$$

These two conditions ensure both momentum conservation and second order accuracy in the total energy conservation [27], provided that the velocity gradient is also calculated using the modified gradient of the shape function as defined in Eq. (7). Although Eq. (6) is in a form that facilitates a discussion of its numerical properties, in practice, the nodal internal force is calculated using Eq. (4). Compared to the original MPM, DDMP requires additional mappings between the material points and corresponding nodes, making it more computationally expensive [27]. However, these additional mappings do not impose any geometric restrictions, so DDMP can be used on unstructured meshes. Interested readers are referred to [27] for details of the additional mappings involved in the DDMP method.

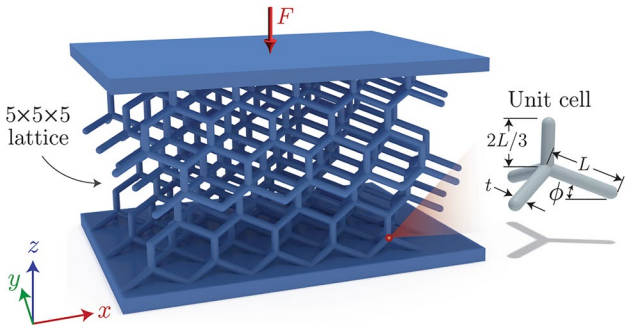

Fig. 1 Illustration of a representative 5×5×5 lattice structure and its corresponding tetrahedral unit cell

As discussed earlier, both the GIMP and DDMP methods offer solutions to mitigate the cell-crossing noise encountered in large deformation analyses, albeit each with its own modifications to the original MPM. In this study, therefore, we aim to verify the numerical solutions by comparing the response features of representative lattice structures using the DDMP and GIMP methods. The verified solutions will then be validated against experimental data from in-lab experiments. Following verification and validation, the proposed computational procedure will then be employed to simulate the behavior of the lattice structures under dynamic loading scenarios for which experimental data are not readily available.

3 Experimental testing of tetrahedral lattice structures

This section presents the results of quasi-static tests conducted on several 5×5×5 tetrahedral lattice structures, whose geometry is shown in Fig. 1. As shown in the figure, each lattice consists of tetrahedral unit cells composed of four cylindrical struts. The three inclined struts are of equal length, L, while the upper (vertical) strut is of length $2L/3$. Each inclined strut forms an angle ϕ with the horizontal plane, and all struts have the same diameter, t. The lattice structures are subjected to a quasi-static compressive force, F.

The dimensions of the lattice structures and details of the fabrication process are provided in Sect. 3.1, followed by a discussion of the loading conditions and the quasi-static compression testing procedures in Sect. 3.2. As shown later, these experimental results serve to validate the GIMP

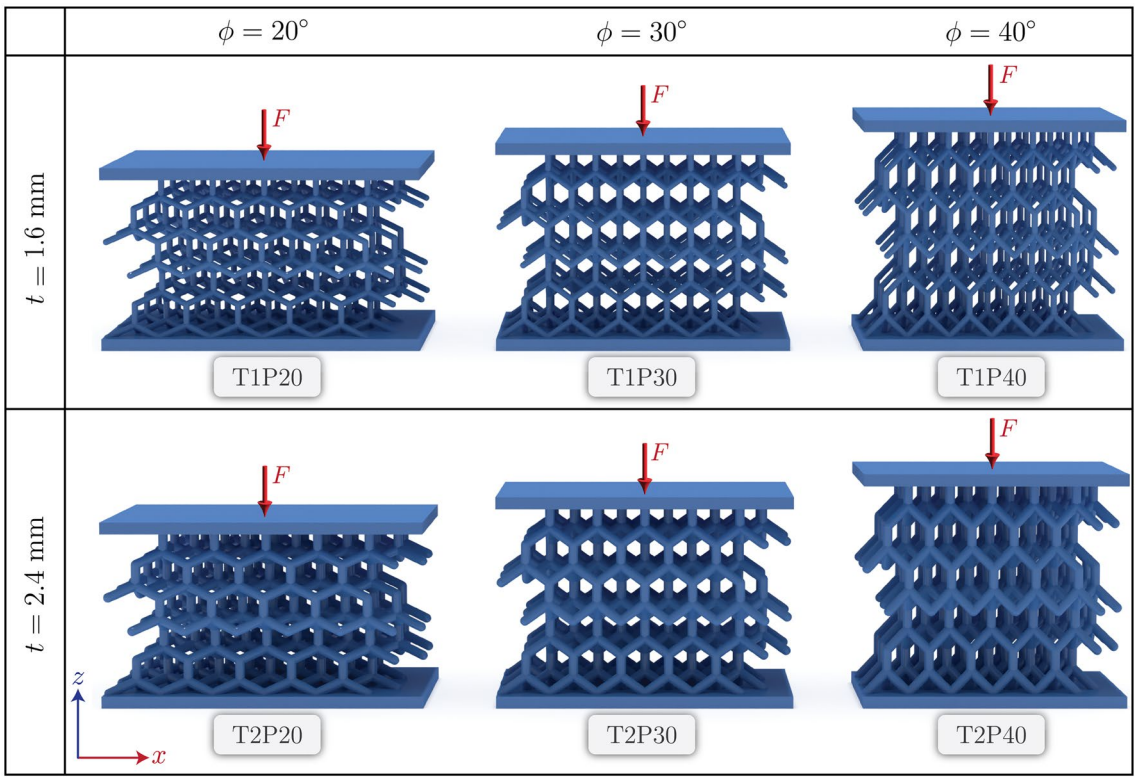

Fig. 2 Tetrahedral lattices with various orientations and strut thicknesses used for the experimental campaign. Lattices labeled with T1 and T2 correspond to strut thicknesses of $t = 1.6$ mm and $t = 2.4$ mm, respectively

and DDMP models by assessing their ability to predict the global and local behaviors of the lattice structures under deformation.

3.1 Fabrication of tetrahedral lattice structures

We used an Original Prusa SL1S SPEED 3D printer to fabricate six variations of the lattice structures depicted in Fig. 1. Each lattice variant combined a specific strut diameter, t, and strut orientation, ϕ, for a fixed strut length, $L = 8$ mm. As detailed in Fig. 2, we considered two strut diameters ($t = 1.6$ mm and $t = 2.4$ mm), and three strut orientations ($\phi = 20°$, $\phi = 30°$, and $\phi = 40°$). These lattice designs were fabricated using the Value UV / DLP Resin Flex from PrimaCreator, which offers a balance between stiffness and flexibility suitable for testing purposes. After printing, the lattice structures were cleaned with isopropyl alcohol to remove any residual uncured resin, followed by drying and curing under UV-light in a CW1S machine. Specifically, the specimens were placed in the chamber which heated to 50 °C, then they were dried for 5 min and subsequently cured for 5 min. Once cured, the specimens were stored in an opaque container to reduce exposure to light, ensuring optimal conditions for further testing. Before testing, the lattices were conditioned at standard laboratory atmosphere in accordance with Procedure A of the ASTM D618 standard. To facilitate testing, 3 mm-thick plates were added at the top and bottom ends of the lattices (see Fig. 2). Moreover, to reduce the impact of manufacturing imperfections, the lattices were printed at a 30° angle (see Fig. S1). A picture of an actual 3D printed lattice is shown in Fig. S2.

To facilitate the identification of the lattices in the sections that follow, we adopted the naming convention TXPY. In this system, X indicates the lattice type, with 1 representing the lattices with a strut thickness of 1.6 mm and 2 representing the lattices with a strut thickness of 2.4 mm. Moreover, Y represents the strut orientation (i.e., 20°, 30°, or 40°). To illustrate, a specimen labeled "T1P30" has a strut thickness of 1.6 mm and strut orientation of 30°.

3.2 Quasi-static compression testing of tetrahedral lattice structures

Prior to performing the quasi-static compression tests on the lattice structures, we first characterized the base material. This was achieved via uniaxial compression tests. To that end, solid cylindrical test specimens of 20 mm in diameter and 60 mm in length were 3D printed and conditioned following the protocol discussed previously. The tests

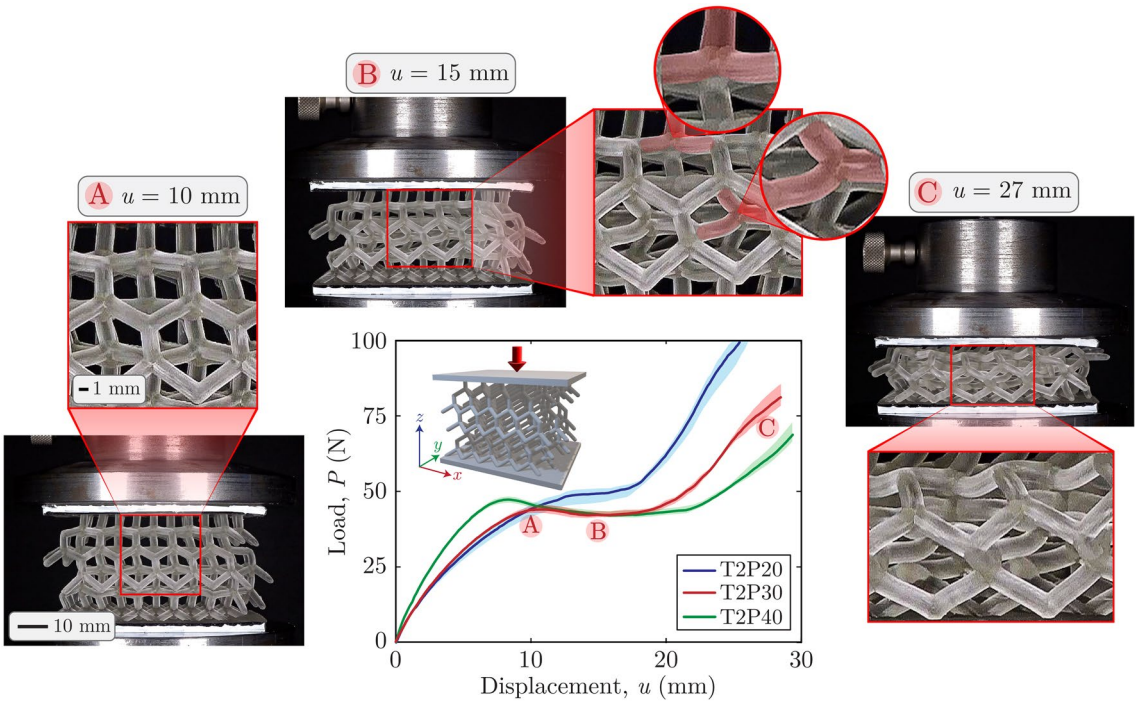

Fig. 3 Response of the T2P20–T2P40 lattice structures under quasi-static compression. Outsets A–C show snapshots of the T2P30 lattice at different deformation levels: (A) shows the deformation at the peak load, (B) at 50% of strain, and (C) at 90% of strain. The inset shows average load–deflection curves of the T2PY lattices

were performed on an ADMET universal testing machine at a controlled displacement rate of 0.003 mm/min, which resulted in a measured Young's modulus of approximately 9.2 MPa (see Figs. S4 and S5).[2]

After characterization of the base material, the previously discussed lattice variations were subjected to quasi-static compression using the same ADMET universal testing machine. The machine was equipped with a 2 kN load cell and two flat plates to ensure uniform application of the compressive load. Moreover, the plates were lubricated with oil to approximate purely uniaxial compression boundary conditions. To ensure data reliability, we printed three identical specimens of each of the lattices shown in Fig. 2, resulting in a total of 18 specimens for testing (refer to Fig. S4 in the supplementary information for additional information about the experimental testing setup). The quasi-static tests were conducted at a constant displacement rate of 0.05 mm/s, and the resulting load–deflection curves were obtained by measuring the force reaction at the top plate. Furthermore, a digital camera was used to record the tests for subsequent analysis.

Figure 3 displays the experimental load–deflection curves obtained for all the T2PY specimens (i.e., those with strut diameter, $t = 2.4$ mm, and strut angles $\phi = 20°$, 30°, and 40°), along with snapshots depicting the deformed shape of the T2P30 lattice during one of the quasi-static tests. Results for all the other lattices considered in the present study are shown in Figs. S6–S8. The graphs reveal a common pattern in the behavior of the lattices characterized by a rapid increase in the load until reaching a peak value, followed by a plateau region, and then by a hardening region. In the plateau region, we observed significant deformation of the lattices, alongside minimal variations in the load level and progressive buckling of the struts. Specifically, at a deflection of about 15 mm, buckling or initial buckling of several struts was observed across all lattices.[3] As the load–displacement curves transition into the hardening region, they exhibit a steep upward trend as the structure densifies, shifting from a cellular to a solid-like state.

[2] To account for potential variability in material properties and experimental uncertainty, the numerical simulations conducted in the following sections assume Young's modulus values of either 8 MPa or 10 MPa. This allowed us to explore the sensitivity of our numerical results to variations in material stiffness. Moreover, a Poisson's ratio of 0.4 was assumed for the simulations based on the values for similar materials.

[3] The buckling behavior in this phase can be classified as predominantly elastic, as the structures returned to their original shape after load removal, indicating no permanent deformation (see Figs S9 and S10).

During the hardening phase, the struts come into contact with one another, and the specific arrangement of the unit cells causes the struts to push against each other, contributing to the increased stiffness and hardening of the material. This interaction between the struts plays a significant role in the densification process, leading primarily to geometric nonlinearities in the overall response of the lattices. Since the lattices returned to their original shape after load removal (see Figs. S9 and S10), material inelasticity (e.g., damage or plasticity) is minimal and does not significantly contribute to the overall behavior. The global nonlinear nature of the load–displacement behavior shown in Fig. 3 reflects the combined effects of progressive buckling, geometric changes, and contact between the struts during densification. While individual struts exhibit primarily elastic buckling at the local level, the hardening phase introduces more complex nonlinear behavior as the structure transitions into a densified state.

Interestingly, the results reveal that the 20° lattices densified at smaller deflections compared to their 30° and 40° counterparts. Specifically, the onset of densification for the 20° lattices occurred at a deflection of approximately 17 mm, while that for the 30° and 40° lattices occurred at deflections of approximately 20 mm and 23 mm, respectively. This early densification in the 20° lattices is attributed to their shallower angle, which results in contact between struts occurring at smaller deflection levels.

4 Comparison between GIMP and DDMP results for simplified models

The experimental findings from the previous section indicate that the lattice structures undergo large deformations and exhibit progressive buckling of the struts as they deform (e.g., see Fig. 3). This buckling phenomenon plays a critical role in understanding the overall behavior of the lattices and has significant implications in their load-bearing capacity. Therefore, prior to modeling the lattices, our initial focus is on examining the ability of the GIMP and DDMP methods to predict the buckling response of slender columns subjected to slow-speed loading aimed to simulate quasi-static loading conditions, such as those considered in the experiments discussed previously. These results will serve as a verification step, enabling us to evaluate the predictive ability of both methods.

We considered a solid cylindrical column with two different diameters, $t = 1.6$ mm and $t = 2.4$ mm, corresponding to the diameters of the lattice struts (see Sect. 3.1). To trigger a smooth buckling response, we introduced initial geometric imperfections in the form of $u_0 = a\sin(\pi z/L)$,[4] where a is the initial deflection at the mid-point and $L = 16$ mm is the length of the column (Fig. 4a). We considered both the case of a perfectly straight column (i.e., $a = 0$) and one with a small geometric imperfection (i.e., $a = 0.02L$). To ensure stability and to prevent rigid-body motion, the bottom end was fixed, and a rigid compressing plate was used at the top of the column to apply a downward force with a constant speed, v_0. To apply these boundary conditions, the bottom material points (shown in blue in Fig. 4) are fixed in place (zero velocity), while the top material points (also shown in blue in Fig. 4) are moved downward at a constant speed. These boundary material points have a significantly higher density (by a factor of 10^6) compared to those of the column to prevent interpenetration between the compressing plates and the column. This approach ensures consistent and controlled loading conditions across all simulations.

We considered two loading speeds, $v_0 = 100$ mm/s and 50 mm/s, to study their influence on the predicted buckling response. The columns are made of a linearly elastic material with Young's modulus, $E = 10$ MPa—close to that of the base material described in Sect. 3.2. The cell size for the buckling simulations is 0.2 mm, while the initial particle spacing is 0.1 mm.[5] Moreover, the numerical models consider a mass density of $\rho = 6\rho_0$, where $\rho_0 = 1.05 \times 10^3$ kg/m^3 is the density reported on the technical datasheet of the base material. This density increase is not expected to alter the buckling response because a quasi-static deformation is independent of the material density. Numerically, the density increase enables us to reduce the wave speed, consequently enabling a larger time step size, which in turn reduces computation time.[6]

Figure 4a illustrates the problem setup and boundary conditions. Figure 4b and c depict the sequence of deformations for the 2.4 mm and 1.6 mm cases, respectively. Figure 4b shows the deformed shape when no imperfections are considered, while Fig. 4c shows the deformed shape when an initial geometric imperfection of $a = 0.02L$ is considered.

Figure 5 shows all the numerical results obtained with the DDMP and GIMP methods alongside the theoretical

[4] The initial geometric imperfection is added solely to trigger a smooth buckling response. Thus, the initial imperfection, $u_0 = a\sin(\pi z/L)$, is not meant to represent a buckling shape or eigenmode [38]. While the sinusoidal shape was selected, other forms, such as a parabolic imperfection, could also be employed to achieve similar results [39–41].

[5] A mesh resolution convergence study was performed that varied the cell size from 0.64 mm to 0.1 mm. The results from this are shown in Fig. 5c.

[6] Both the GIMP and DDMP codes use explicit time integration for dynamic analysis. In this context, the quasi-static problems simulated herein are approached as dynamic problems with a low loading rate.

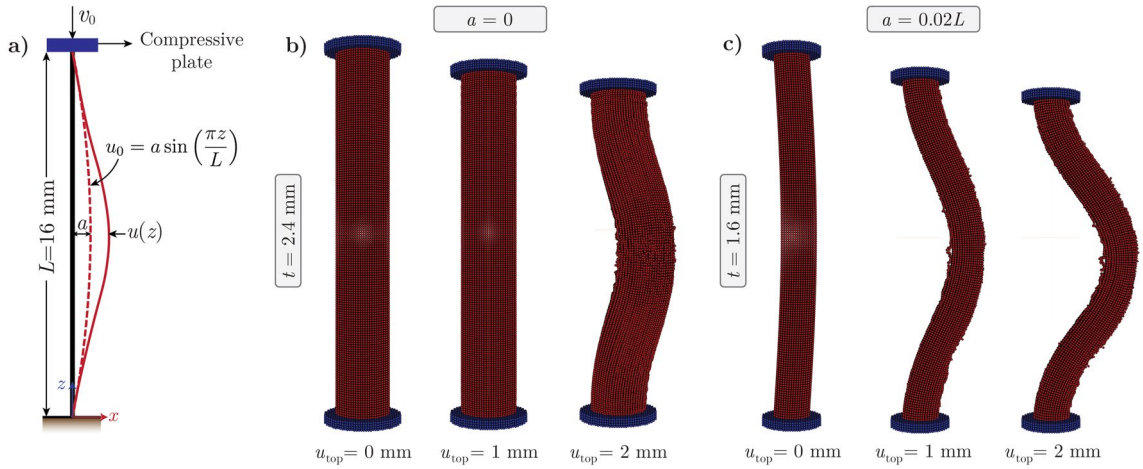

Fig. 4 Buckling behavior of two slender columns obtained with the DDMP method: (**a**) column geometry and boundary conditions; (**b**) DDMP model of progressive deformation of a column without initial geometric imperfection ($a = 0$) and diameter $t = 2.4$ mm at different top displacements, u_{top}; and (**c**) DDMP model of progressive deformation of a column with initial geometric imperfection ($a = 0.02L$) and diameter $t = 1.6$ mm at different top displacements, u_{top}

values corresponding to the Euler buckling loads for the two different diameters. As observed, when no geometric imperfection is considered (i.e., $a = 0$), both methods overpredict the critical load (Fig. 5a, b). In these cases, the columns eventually buckle and oscillate around the theoretical critical load. This behavior is attributed to numerical roundoff errors inherent in any numerical model. In an ideal scenario with no numerical errors, the columns would compress infinitely without buckling. However, since numerical errors are inevitable, they introduce the instability that leads to the observed buckling behavior. As shown in Fig. 5a, b, the overprediction of the DDMP models exhibits a closer trend to the Euler load after buckling onset, while the GIMP predictions deviate more significantly. Similar results were observed for the 2.4 mm diameter cases but have been omitted from Fig. 5a, b for clarity.

As shown in Fig. 5c, d, when a small geometric imperfection is introduced (i.e., $a = 0.02L$), the results from both methods approach the theoretical critical buckling load. For the 1.6 mm case, both the DDMP and GIMP methods closely approximate the theoretical critical load, but they slightly overestimate it for the 2.4 mm case. This overestimation is not unexpected, as Euler's theory does not account for factors such as inertia or the finite thickness of the column. Additionally, as shown in Fig. 5d, reducing the speed to $v_0 = 50$ mm/s brings the results even closer to the theoretical critical load for both methods, as lower speeds better approximate quasi-static loading conditions.

To further verify our MPM results, we also performed finite element buckling simulations using ANSYS. We focused on the 2.4 mm case and considered an initial velocity of $v_0 = 100$ mm/s and $a = 0.02L$. The material was modeled as linear elastic, using the properties described previously. The column was discretized with four-node tetrahedral elements, fixed at the base, and subjected to a velocity boundary condition at the top in the negative z direction. Lateral movement in the xy-plane was constrained, allowing only vertical displacement of the top surface. As shown in Fig. 5e, the load vs. displacement results from the FEM simulations align closely with those obtained using the DDMP method.

In addition to displaying the finite element results, Fig. 5e also displays the results of a cell size convergence analysis performed using the DDMP method. This analysis compares the results obtained for cell sizes of 0.1 mm, 0.2 mm, 0.4 mm, and 0.64 mm, where the latter is the cell size used for the full lattice models, as discussed later in this manuscript. Our findings indicate minimal differences between the 0.1 mm and 0.2 mm cases. While the 0.4 mm and 0.64 mm cases slightly underestimate the results compared to the finer resolutions, the overall behavior remains consistent across all tested scales.

The findings discussed in this section confirm the ability of both the DDMP and GIMP methods to predict the buckling response of slender members, thereby instilling confidence in their ability to simulate the response of complex lattice structures undergoing buckling.

5 Validation of GIMP and DDMP results for tetrahedral lattice structures

In this section, we employ the DDMP and GIMP methods to simulate the quasi-static response of the lattice structures depicted in Fig. 2 and compare the simulated results against

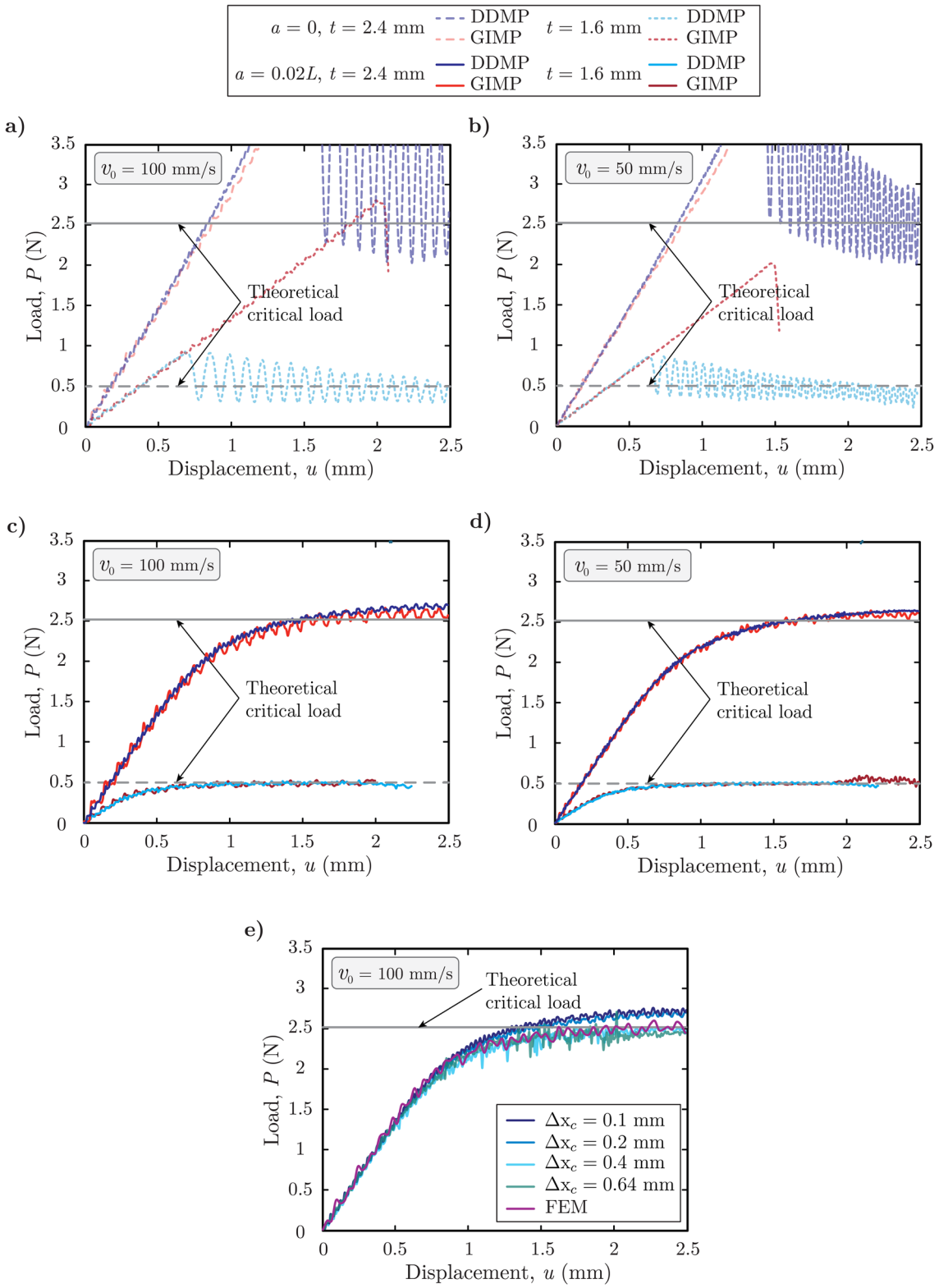

Fig. 5 Comparative load–displacement curves from buckling analysis of slender columns. (**a**), (**b**) DDMP vs. GIMP results for $v_0 = 100$ mm/s (**a**) and $v_0 = 50$ mm/s (**b**) for the unperturbed case $a = 0$, (**c**), (**d**) DDMP vs. GIMP results for $v_0 = 100$ mm/s (**c**) and $v_0 = 50$ mm/s (**d**) for the perturbed case $a = 0.02L$, (**e**) DDMP results from cell size analysis and FEM results for column with $t = 2.4$ mm and $v_0 = 100$ mm/s

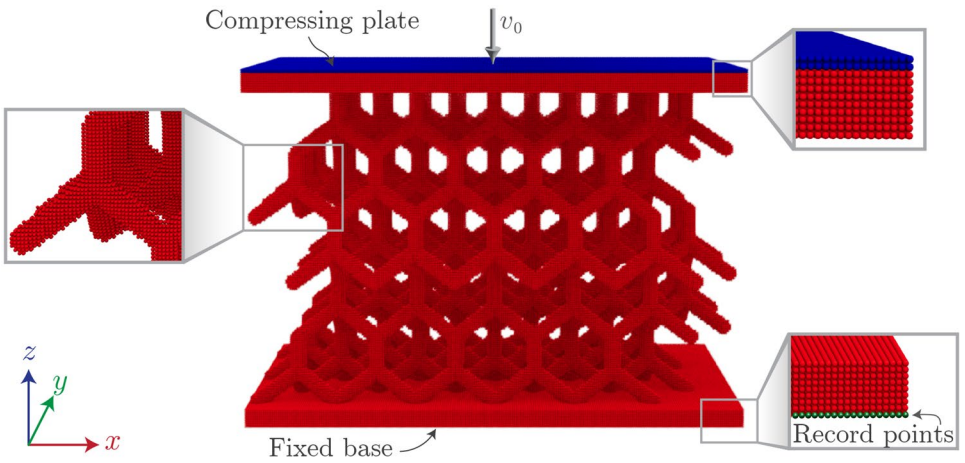

Fig. 6 Schematic representation of a tetrahedral lattice model (T2P30) using the DDMP or GIMP methods

the experimental results discussed previously. Initially, we provide a description of the DDMP and GIMP lattice models, followed by a comparison between the numerical and experimental results. At the end of this section, we discuss results from additional lattice models that account for various types of geometric imperfections, herein referred to as perturbations. These additional models aim to explain discrepancies observed between the results obtained with the original set of models and the experimental results.

5.1 Simulation model set up

In this section, we present details of the DDMP and GIMP models of the lattice structures discussed in Sect. 3. Figure 6 illustrates a representative numerical model featuring a lattice structure fixed at the bottom and a compressing plate located at the top. The compressive plate moves downward at a constant speed of $v_0 = 100$ mm/s. A layer of record points is specified at the base to measure the reaction force during each simulation. We subdivided the models into grid cells in the xyz space with spacing of 0.64 mm in each direction. Each cell is assigned two material points along each direction, resulting in a total of eight material points within a cell when initially filled with material.

As discussed in the previous section, we also adopted a mass density of $\rho = 6\rho_0$, with $\rho_0 = 1.05 \times 10^3$ kg/m^3 for the lattices to reduce the overall computation time. We assumed a linear elastic material model for the lattice. Herein, we considered two different values for the Young's modulus ($E = 8$ MPa and $E = 10$ MPa) and treated the flyer as a rigid body with a significantly higher density than that of the lattice (similar to the buckling simulation discussed in the previous section). A zero-velocity boundary condition was applied to the bottom of the lattice structures. In our DDMP simulations, we computed the reaction force using the method discussed in [37]. Conversely, for the GIMP simulations, we measured the reaction force by averaging the stress along the bottom layer of material points, labeled as record points in Fig. 6.

5.2 Numerical results for lattices without initial geometric imperfections

Figure 7 compares the numerical results obtained with the DDMP and GIMP models to the range of experimental results for the six lattice structures discussed in Sect. 3. As observed in the figure, the load–displacement responses predicted by both DDMP and GIMP models approximate those measured experimentally for most of the lattices, up to a displacement of approximately $u = 5 - 10$ mm. Beyond this point, the numerical and experimental results differ in most of the cases. As Fig. 7 shows, for the T1 lattices, the results obtained with $E = 10$ MPa better approximate the experimental load–displacement response than those obtained with $E = 8$ MPa. Moreover, for the T2 lattices, the results obtained with $E = 10$ MPa capture the peak load better, while those obtained with $E = 8$ MPa better capture the post-peak response. These results suggest that a Young's modulus of $E = 10$ MPa provides a better approximation of the initial part of the curves up to the peak load, but significant differences are observed in the post-peak regime due to the potential interaction between geometrical and material instabilities (beyond the scope of this paper).

In an attempt to understand the discrepancies between the numerical and experimental results observed in Fig. 7, we considered a representative lattice structure and compared the deformed shapes obtained from the DDMP and GIMP models with those obtained experimentally. Figure 8 shows such a comparison for the T2P30 lattice at three displacement levels: $u = 0$, 10 mm, and 20 mm. A comparison of the numerical and experimental results for the remaining lattice structures is provided in Figs. S11–S16. As shown by the results, both numerical models can capture the deformation pattern accurately at $u = 10$ mm. However,

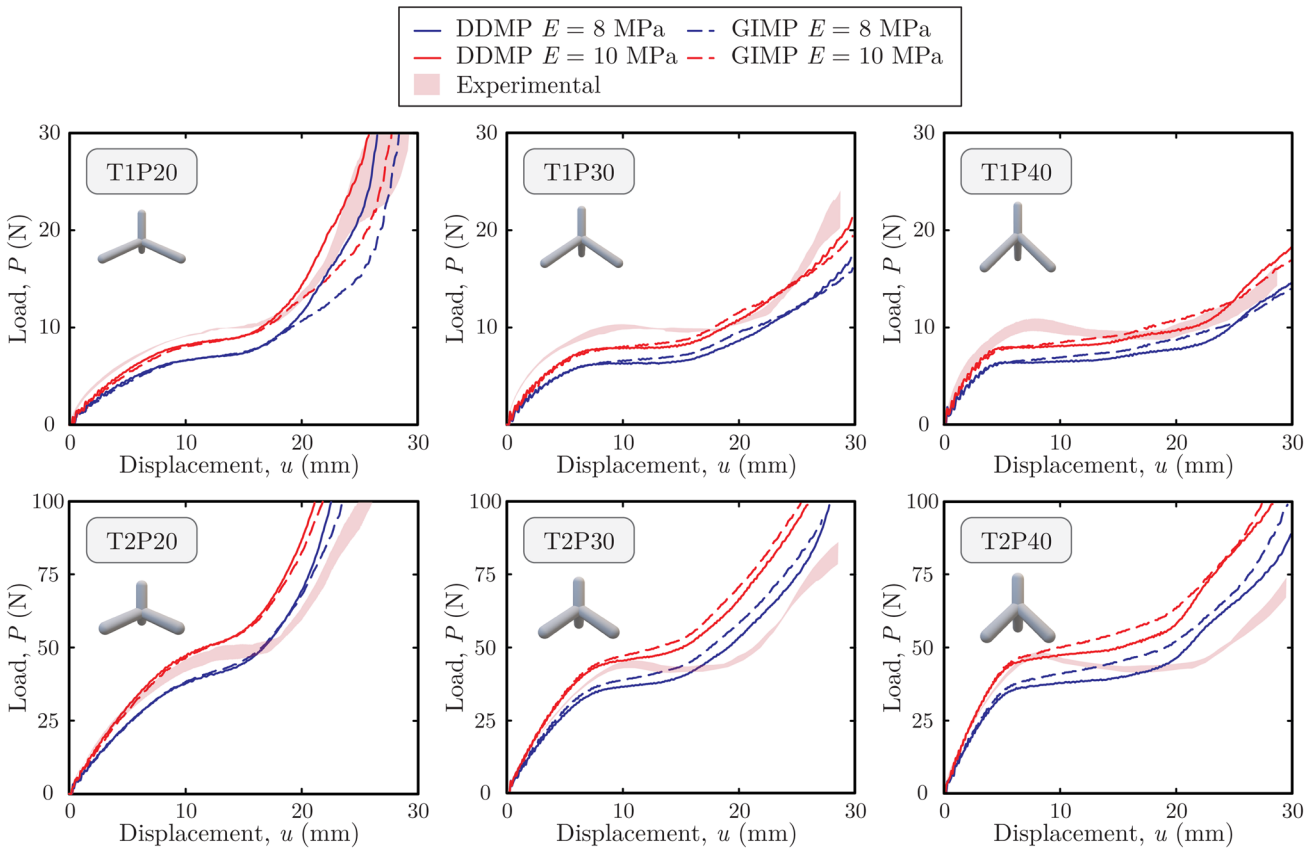

Fig. 7 Load–displacement curves obtained using the GIMP and DDMP methods for the two different Young's moduli, $E = 8$ MPa and $E = 10$ MPa, with the T1PY lattices (top) and T2PY lattices (bottom)

at $u = 20$ mm, most unit cells have buckled in different ways, resulting in discrepancies between the experimental and the numerical results. A notable discrepancy emerges at the top layer of the lattice (i.e., the layer of unit cells in contact with the top plate), which tends to tilt to the right in the experiments, whereas this effect is less pronounced in the numerical models. These differences, which may be attributed to initial imperfections in the lattices that occurred during 3D printing, may explain the differences between the load–displacement results discussed earlier. Despite these discrepancies, our numerical models effectively capture the different deformation patterns observed in the experiments, even though we did not account for the interaction between geometric and material nonlinearities.

5.3 Numerical results for lattices with initial geometric imperfections

The numerical results discussed in the previous section assume the lattices are free of initial geometric imperfections. However, this assumption leads to inaccuracies in predicting deformation patterns at higher deformation levels, as seen in Fig. 8. These inaccuracies are reflected in an overestimation of the load in the post-peak regime, as illustrated in Fig. 7. Visual inspection of our 3D-printed lattices revealed that some geometric imperfections occurred during 3D printing. These imperfections, which are often manifested in the form of curved members, may trigger specific deformation responses when the lattices undergo loading. However, such responses cannot be accurately captured by the numerical models unless they also consider initial imperfections. Due to our inability to precisely measure the geometric imperfections beyond qualitative assessments from visual inspections, this section uses the DDMP and GIMP methods to explore how different types of geometric imperfections, herein referred to as *perturbations*, could affect the global response of the lattice structures.

Figure 9 presents a schematic illustration of the base lattice configuration along with four types of perturbations considered in this section. Three additional types of perturbations were also considered, but they had a negligible effect on the results. Description of these additional perturbations, alongside numerical results obtained with the DDMP models, can be found in the supplementary information (refer to Figs. S17–S18). As seen in the base configuration, the structure consists of five vertical layers of unit cells, each

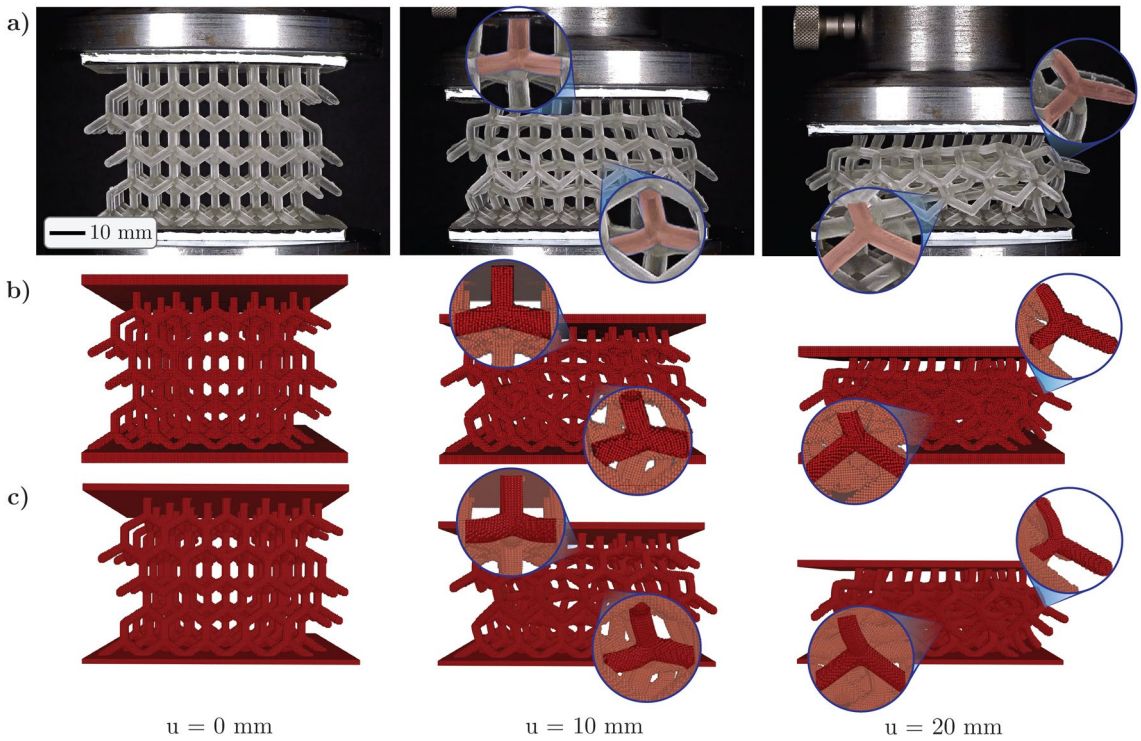

Fig. 8 Progressive deformation of the T2P30 lattice at three different displacement levels: $u = 0$, 10, and 20 mm. (**a**) Experimental results, (**b**) results from the DDMP method, and (**c**) results from the GIMP method

layer containing a 5×5 arrangement of unit cells perpendicular to the compression direction, and two base regions, representing the top and bottom plates added for testing, and the compressing plate.[7] A zoomed-in view of the base material point configuration highlights the perfectly aligned material points before introducing any perturbation. As in the previous simulations, the cell spacing is 0.64 mm, and the material point spacing is 0.32 mm. The perturbations affect only the lattice structure and the base regions, while the compressing plate remains unperturbed in all variations. In this section, we only considered the T1P40 lattice. Each of the perturbations is described as follows:

- *Perturbation A—slanted top layer*. The first type of perturbation involved slanting the top (fifth) layer of the lattice structure to investigate the induction of the buckling mode observed in Fig. 8. The total slant for the top layer was 1.28 mm (twice the cell size).
- *Perturbation B—slanted lattice*. The second type of perturbation involved slanting the entire lattice in a direction perpendicular to the compression direction, based on visual observations of the 3D-printed samples, which showed a slight inclination ranging from 1.0 mm to 1.5 mm. To reflect this, a total slant of 1.28 mm was applied in the simulation, representing twice the cell size and falling within the observed range of the fabricated lattices. This perturbation aimed to investigate the effect of such inclination on the lattice behavior.
- *Perturbation C—curved top base*. The third type of perturbation introduced initial curvature in the top base, inspired by experimental observations of detachment between the compression plate and the top base (see Fig. 8a). The curvature is such that the maximum detachment distance between the compression plate and the top base structure was 1.28 mm.
- *Perturbation D—bowed lattice*. The fourth type of perturbation simulated bowing of the lattice, accounting for minor deviations in manufacturing alignment due to gravity. The bowing was designed to produce a maximum imperfection of 1.28 mm at the midpoint between the top and bottom bases.

Figure 10 shows the load–displacement results obtained with the DDMP and GIMP methods from the models considering the perturbation cases applied to the T1P40 lattice. As observed from the figures, up to a displacement of 15 mm, all perturbations have a minimal impact on the load–displacement response. However, as the deformation increases, perturbations can significantly affect the post-peak

[7] The base configuration essentially corresponds to the schematic model shown in Fig. 6.

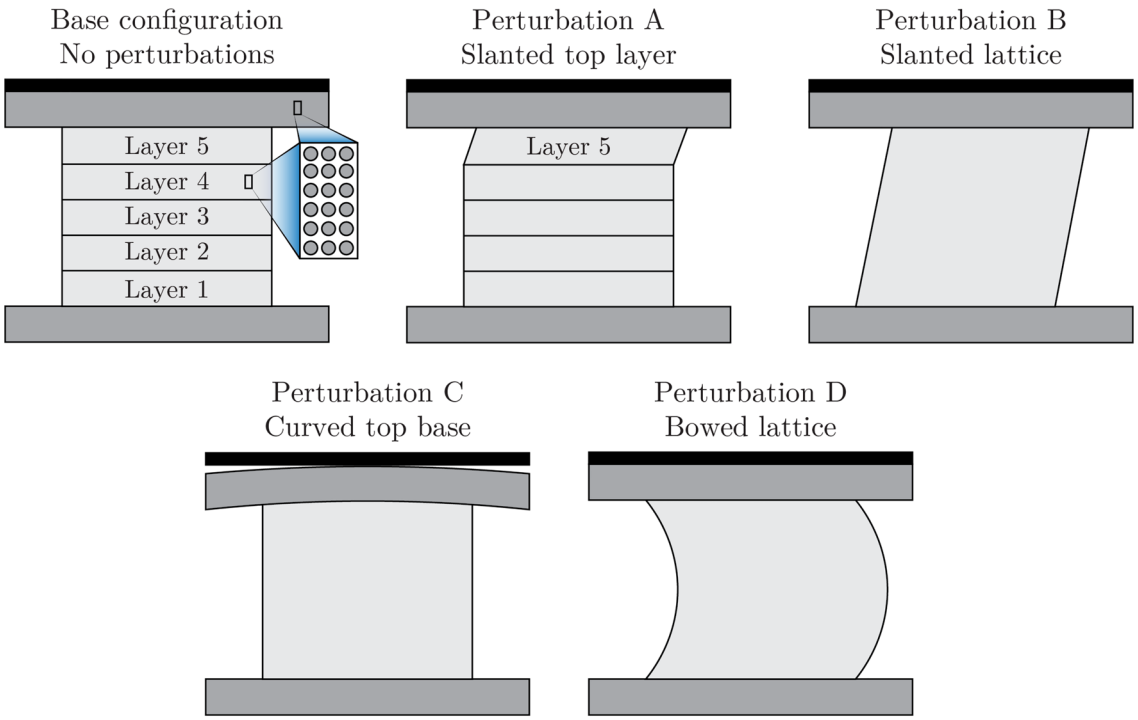

Fig. 9 Base lattice configuration along with four different types of perturbations (**A**–**D**) considered for the imperfection analysis

response. These perturbations correspond to either larger-scale imperfections that arise during the printing of the entire lattices (perturbations A, B, and D) or issues that arise during the experiments, as in perturbation C. Larger-scale perturbations can either increase the force displacement response as in perturbation C, or decrease the response, as in perturbation D. These perturbations alter the buckling modes, affecting the post-buckling response of the entire lattice. By introducing larger-scale imperfections and defects, the numerical models better capture the post-peak response and buckling modes, resulting in a closer match to the behavior of the actual lattices.

Although accounting for initial geometric imperfections helped align our numerical results more closely with the experimental ones, Fig. 10 still shows considerable differences between the numerical and experimental results. One probable factor influencing the accuracy of our numerical results is the assumption that the base material exhibits a linear elastic behavior. While we acknowledge that incorporating material nonlinearities (e.g., a hyperelastic material model) and/or viscoelasticity may improve the approximation of the experimental responses, exploring these aspects falls beyond the scope of the current study.

6 Engineering representative lattice structures with verified and validated codes

Following the quasi-static simulations, we conducted dynamic simulations to investigate the response of the lattice structures under impact loading. The computational models created in this section are based on the lattice geometries depicted in Fig. 2. The lattices are impacted by a rigid, 10-kg flyer, traveling at 2 m/s downward when it begins to impact the lattices. The velocity of the flyer during impact is affected by the resistance of the lattice structure and gravity ($g = 9.81$ m/s^2), providing a realistic representation of dynamic loading conditions. Due to the dynamic nature of the simulations, the actual density of the material ($\rho_0 = 1.05 \times 10^3$ kg/m^3) was used for the lattice. Two Young's moduli are considered ($E = 10$ MPa and $E = 100$ MPa), and the Poisson's ratio is taken as $\nu = 0.4$, in order to investigate the effect of material properties on the energy absorption of the lattices under large, dynamic deformations. Understanding the energy absorption of these structures would allow one to tune these metamaterials to specific applications. The following discussion aims to provide an initial insight into the potential of using tetrahedral lattice structures for impact resistance applications. Additionally, numerical simulation results for cases in which the lattices undergo complete densification should be interpreted with

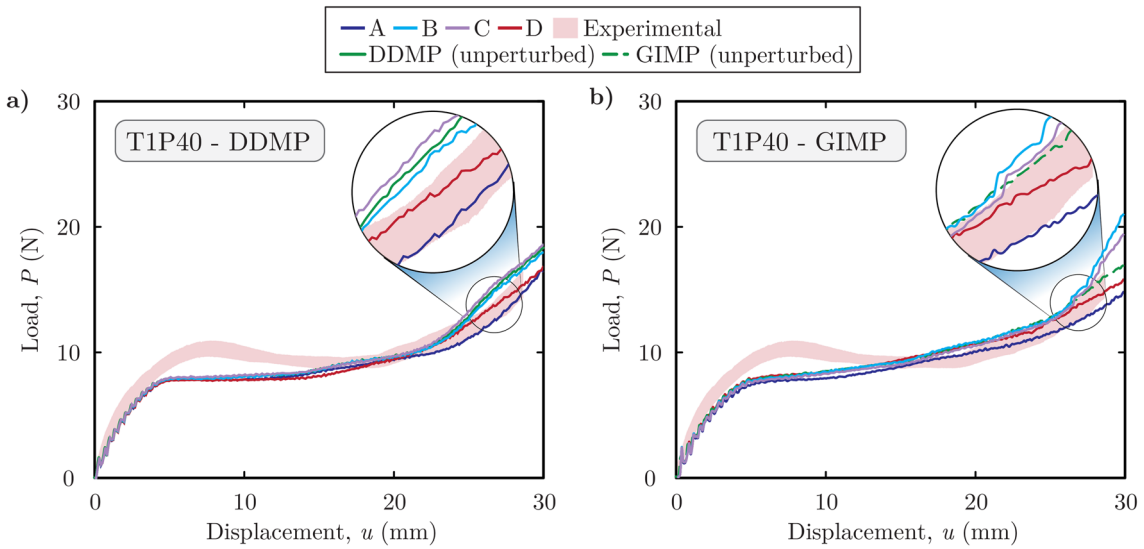

Fig. 10 Load–displacement curves obtained from the geometric imperfection analysis of the T1P40 lattice: (**a**) DDMP results and (**b**) GIMP results

caution, particularly after rebound, as none of the models directly account for frictional contact.

Figures 11a, b and 12a, b display the time responses of the load as obtained with the DDMP and GIMP methods for the different lattice structures. In the cases of soft lattices ($E = 10$ MPa with $t = 1.6$ mm and $t = 2.4$ mm) and thin, stiff lattices ($E = 100$ MPa and $t = 1.6$ mm), a sharp peak appears in the curves. However, for the stiff, thick lattices ($E = 100$ MPa and $t = 2.4$ mm), a plateau precedes the formation of a more gradual peak. The peaks occur as the lattice structures nearly reach complete densification, with individual unit cells deforming and coming into contact with each other. In other words, the lattice structures have completely folded into the empty space between the top and bottom of the lattice. For the thicker and stiffer lattices (i.e., those corresponding to $E = 100$ MPa and $t = 2.4$ mm), although they still undergo a large deformation and begin to densify, their increased stiffness enables them to absorb the energy of the flyer before they begin to push it back upward.

For the cases where the lattice completely folds upon itself, the flyer speed drops sharply before increasing again as the flyer changes direction, which occurs between 15 and 25 ms depending on the lattice, as shown in Figs. 11c, d and 12c. However, for the stiff, thick lattices, as shown in Fig. 12d, the flyer speed decreases gradually between 0 and 15 ms, after which the speed decreases rapidly.

Both DDMP and GIMP models exhibit sharp peaks in the load, particularly in the softer cases, with most of the DDMP peaks being higher and occurring slightly earlier than the GIMP peaks. Although both methods initially display similar characteristics for the stiffest case (Fig. 12b) at early times (below ~ 15 ms), they start to diverge as time progresses. One possible explanation for these differences could be how DDMP and GIMP handle buckling, as shown by the numerical results in Sect. 4. Another possible explanation could be that as the lattices undergo large deformations, the individual struts begin to come into contact with one another. Since DDMP and GIMP have different support regions for a node, contact between two struts may occur earlier in the DDMP due to its larger support region compared to GIMP. Moreover, unless contact and friction between individual lattice struts are explicitly modeled, an unphysical "stickiness" begins to occur when the struts come into contact since nonslip contact is inherent in the MPM. This artifact arises due to the interpolation of particle information onto the grid, as a grid node does not differentiate between interpolated data coming from separate struts, and thus it should be handled differently. During the quasi-static tests, no significant slip was observed between the struts as they contacted each other, which suggests that allowing the struts to artificially stick to one another may yield reasonable results, at least until the lattices begin to rebound. Previous studies [20, 23, 33, 34] have proposed methods such as multi-mesh or penalty methods to explicitly handle contact within the MPM. Although these methods are out of the scope of the present study, our team is actively exploring this research area for further improvements in our modeling capabilities. Moreover, we are exploring ways of incorporating further material and geometric nonlinearities to improve the predictive capabilities of our DDMP and GIMP frameworks.

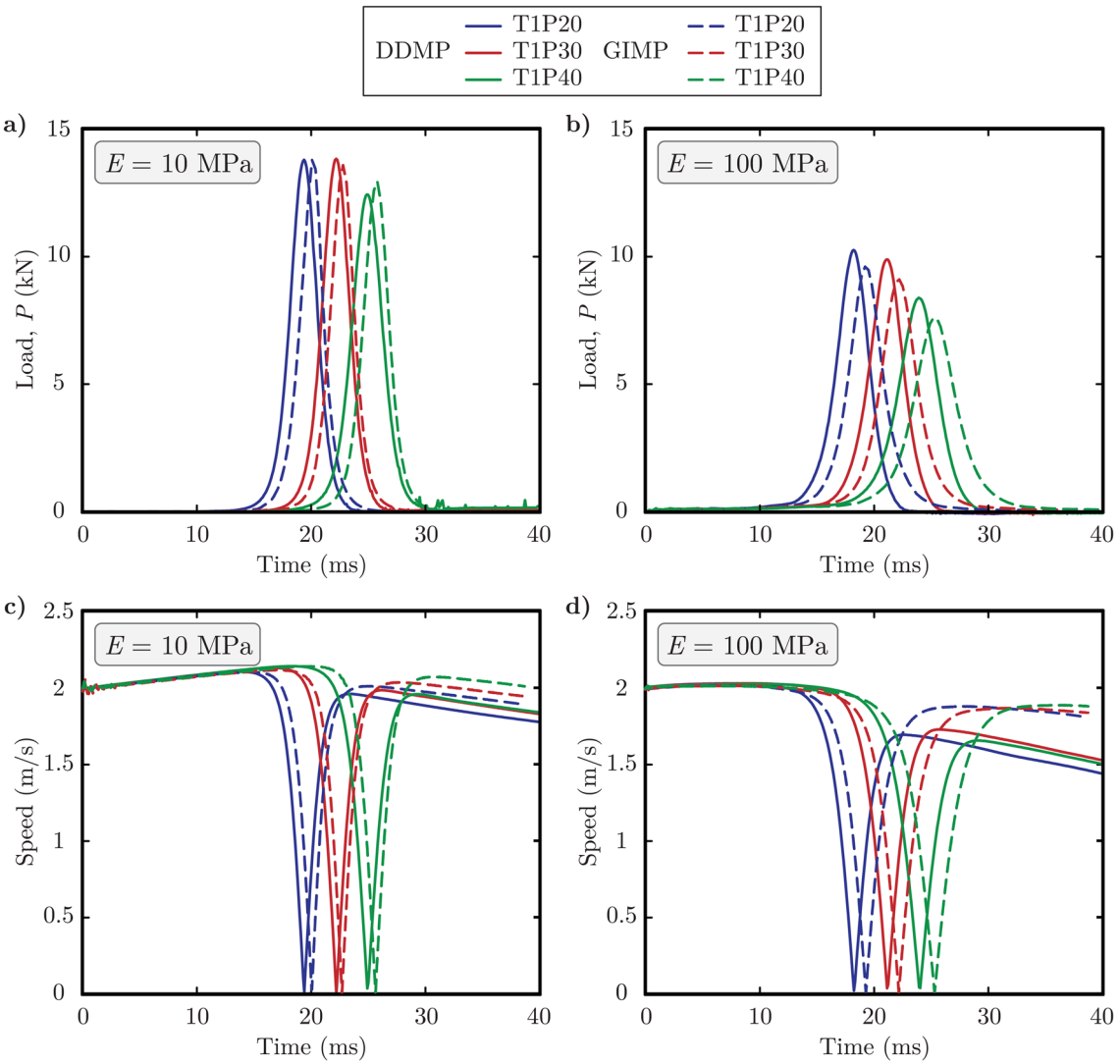

Fig. 11 Dynamic responses of the T1P20–T1P40 lattices obtained with the DDMP and GIMP methods for different values of the Young's modulus, E: (**a**), (**b**) load vs. time response, (**c**), (**d**) speed vs. time response, and (**e**), (**f**) flyer total energy vs. time

7 Concluding remarks and future research tasks

In this study, we have examined the potential of the DDMP and GIMP methods for developing a computational framework tailored to engineering lattice structures subjected to extreme loading conditions. As a first step toward this general objective, we simulated the behavior of several tetrahedral lattice structures under quasi-static loading and compared the numerical results against those obtained experimentally. Interestingly, the results reveal that both the DDMP and GIMP methods are able to capture the experimental load–displacement responses in the pre-buckling regime but start to deviate from the experimental data in the post-bucking regime. By comparing the deformed shapes predicted by the numerical models with those observed from the experiments, we could conclude that both the DDMP and GIMP methods are robust in capturing the deformed shapes before individual strut buckling occurs.

Based on visual inspection of the lattices tested experimentally, it appears that the most likely source of discrepancy between the numerical and experimental results is due to initial geometric imperfections that arise during 3D printing. In an attempt to quantify the effects of initial geometric imperfections, we created a second set of numerical models accounting for different types of perturbations (i.e., imperfections) that reflect experimental observations. The perturbations considered here include slanting either the top layer of the lattices or the entire lattice structures, and applying initial curvatures at the top of the lattice or across the lattice height. The results obtained from the perturbed

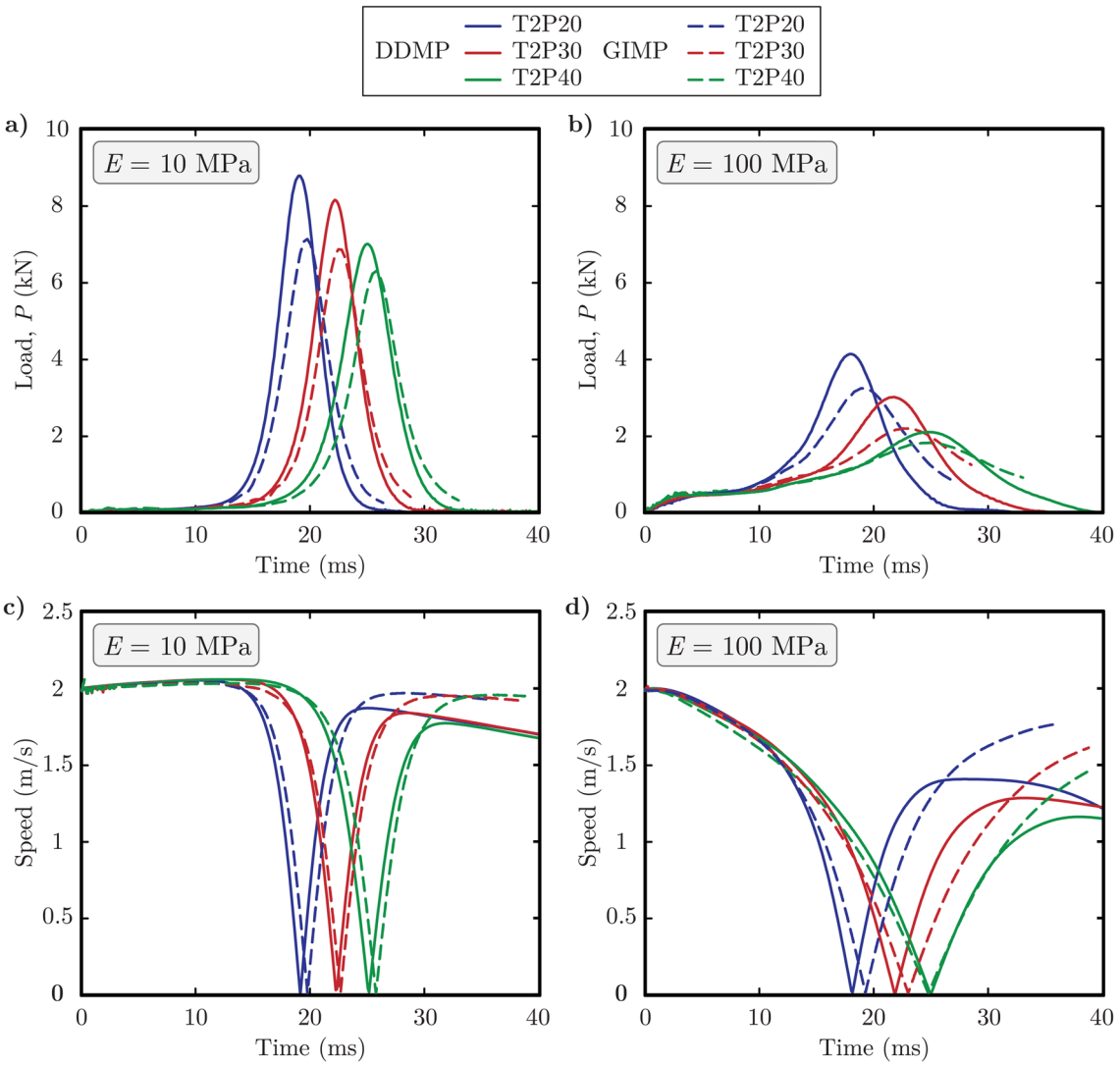

Fig. 12 Dynamic responses of the T2P20–T2P40 lattices obtained with the DDMP and GIMP methods for different values of the Young's modulus, E: (**a**), (**b**) load vs. time response, (**c**), (**d**) speed vs. time response, and (**e**), (**f**) flyer total energy vs. time

models indicate that initial geometric imperfections have a negligible effect on the pre-bucking response, but may have a significant effect on the post-buckling response.

Using the GIMP and DDMP codes verified and validated in the quasi-static loading cases, we then analyzed the responses of the lattice structures under dynamic loading. For the dynamic loading cases, we considered two types of materials, namely, a soft material with a Young's modulus of 10 MPa (similar to the Young's modulus measured for the base material in the quasi-static models) and a stiff material with a Young's modulus of 100 MPa. This allowed us to evaluate the effect of the Young's modulus on the dynamic response of the lattice structures. The numerical results indicate that, for the selected impact speed and flyer mass, stiffer lattices generally lead to a reduction in the peak load experienced during impact as compared to softer lattices. In addition, as the lattice stiffness increases, not only does the peak load decreases, but also the speed of the flyer varies more gradually during impact. Our recent investigation via molecular dynamics has demonstrated that architected materials could significantly affect the damage evolution in protected targets under impact [42]. The current work further motivates the need for multiscale modeling and evaluation of metamaterials under impact loading, for which particle methods appear to be robust in spatial discretization in combination with image processing.

We acknowledge that our modeling framework has certain limitations. For example, our models assume linear elastic material behavior, and frictional effects are not explicitly considered when structs come into contact. While material nonlinearities, inelastic material behavior, detailed contact

formulations, and interactions between material and geometric instabilities are beyond the scope of this study, this work lays the groundwork for applying particle-based methods in engineering lattice structures under extreme loading conditions. Future research will focus on enhancing the proposed computational framework and experimental techniques by addressing the above issues.

Supplementary Information The online version contains supplementary material available at https://doi.org/10.1007/s00366-024-02098-5.

Acknowledgements The authors are grateful for the financial support provided by the Materials Science and Engineering Institute at University of Missouri (MU). Oliver Giraldo-Londoño and Rogelio A. Muñeton-Lopez are grateful for the endowment provided by the James W. and Joan M. O'Neill Faculty Scholar in Engineering at MU. The authors would also like to thank Mr. Chadwick Bettale and Mr. Jacob Smith at MU for their valuable assistance with the experimental phase of this research. Paul L. Barclay and Duan Z. Zhang would like to acknowledge the financial support provided by the Advanced Simulation and Computing (ASC) program, Campaign 2 of Los Alamos National Laboratory, and LDRD program (20230310ER) of Los Alamos. Los Alamos National Laboratory is operated by Triad National Security, LLC, for the National Nuclear Security Administration of U.S. Department of Energy (Contract No. 89233218NCA000001). The findings and opinions expressed in this study solely represent those of the authors and do not necessarily reflect the views of the sponsors or sponsoring agencies.

Author contributions O.G.L. and Z.C. designed the research. R.M.L. and O.G.L. performed the experimental portion of the research, analyzed the results, and created the figures and videos. P.L.B. and D.Z.Z. conducted the numerical simulations using the DDMP method. X.Z. and Z.C. conducted the numerical simulations using the GIMP method. All authors contributed to the manuscript write-up. All authors reviewed the results and approved the final version of the manuscript.

Data availability No datasets were generated or analysed during the current study.

Declarations

Conflict of interest The authors declare no competing interests.

References

1. Surjadi JU, Gao L, Du H, Li X, Xiong X, Fang NX, Lu Y (2019) Mechanical metamaterials and their engineering applications. Adv Eng Mater 21(3):1800864. https://doi.org/10.1002/adem.201800864
2. Portela CM (2019) Fabrication, mechanical characterization, and modeling of 3D architected materials upon static and dynamic loading. Dissertation, California Institute of Technology
3. Pechac JE, Frazier MJ (2022) Metamaterial design strategy for mechanical energy absorption under general loading. Extreme Mech Lett 51:101580. https://doi.org/10.1016/j.eml.2021.101580
4. Injeti SS, Daraio C, Bhattacharya K (2019) Metamaterials with engineered failure load and stiffness. Proc Natl Acad Sci USA 116(48):23960–23965. https://doi.org/10.1073/pnas.1911535116
5. Jia Z, Liu F, Jiang X, Wang L (2020) Engineering lattice metamaterials for extreme property, programmability, and multifunctionality. J Appl Phys 127(15):150901. https://doi.org/10.1063/5.0004724
6. Shan S, Kang SH, Raney JR, Wang P, Fang L, Candido F, Lewis JA, Bertoldi K (2015) Multistable architected materials for trapping elastic strain energy. Adv Mater 27(29):4296–4301. https://doi.org/10.1002/adma.201501708
7. Yang T, Chen H, Jia Z, Deng Z, Chen L, Peterman EM, Weaver JC, Li L (2022) A damage-tolerant, dual-scale, single-crystalline microlattice in the knobby starfish, *Protoreaster nodosus*. Science 375(6581):647–665. https://doi.org/10.1126/science.abj9472
8. Li S, Liu WK (2007) Meshfree particle methods. Springer, Berlin
9. Sulsky D, Chen Z, Schreyer HL (1994) A particle method for history-dependent materials. Comput Methods Appl Mech Eng 118(12):179–196. https://doi.org/10.1016/0045-7825(94)90112-0
10. Chen Z, Brannon RM (2002) An evaluation of the material point method. Sandia National Lab. (SNL-NM), Albuquerque; Sandia National Lab.(SNL-CA). https://doi.org/10.2172/793336
11. De Vaucorbeil A, Nguyen VP, Sinaie S, Wu JY (2020) Chapter two—material point method after 25 years: theory, implementation, and applications. Adv Appl Mech 53:185–398. https://doi.org/10.1016/bs.aams.2019.11.001
12. Sołowski WT, Berzins M, Coombs WM, Guilkey JE, Möller M, Tran QA, Adibaskoro T, Seyedan S, Tielen R, Soga K (2021) Material point method: overview and challenges ahead. Adv Appl Mech 54:113–204. https://doi.org/10.1016/bs.aams.2020.12.002
13. Nguyen VP, de Vaucorbeil A, Bordas S (2023) The material point method: theory, implementations and applications. Springer, Cham
14. Zhang X, Chen Z, Liu Y (2016) The material point method: a continuum-based particle method for extreme loading cases. Academic Press, London
15. Lenardic A, Moresi L, Mühlhaus H (2000) The role of mobile belts for the longevity of deep cratonic lithosphere: the crumple zone model. Geophys Res Lett 27(8):1235–1238. https://doi.org/10.1029/1999GL008410
16. Więckowski Z, Youn SK, Yeon JH (1999) A particle-in-cell solution to the silo discharging problem. Int J Numer Methods Eng 45:1203–1225
17. York AR, Sulsky D, Schreyer HL (1999) The material point method for simulation of thin membranes. Int J Numer Methods Eng 44(10):1429–1456
18. Zhou S, Stormont J, Chen Z (1999) Simulation of geomembrane response to settlement in landfills by using the material point method. Int J Numer Anal Methods Geomech 23:1977–1994
19. Sulsky D, Schreyer HL (1996) Axisymmetric form of the material point method with applications to upsetting and Taylor impact problems. Comput Methods Appl Mech Eng 139(1):409–429. https://doi.org/10.1016/S0045-7825(96)01091-2

20. Sulsky D, Zhou SJ, Schreyer HL (1995) Application of a particle-in-cell method to solid mechanics. Comput Phys Commun 87(1):236–252. https://doi.org/10.1016/0010-4655(94)00170-7
21. Bardenhagen SG, Harstad EN, Maudlin PJ, Gray GT, Foster JC Jr (1998) Viscoelastic models for explosive binder materials. AIP Conf Proc 429:281–284. https://doi.org/10.1063/1.55647
22. Bardenhagen SG, Brackbill JU (1998) Dynamic stress bridging in granular material. J Appl Phys 83(11):5732–5740. https://doi.org/10.1063/1.367429
23. Bardenhagen SG, Brackbill JU, Sulsky D (2000) The material-point method for granular materials. Comput Methods Appl Mech Eng 187(3):529–541. https://doi.org/10.1016/S0045-7825(99)00338-2
24. Bardenhagen SG, Brackbill JU, Sulsky D (2000) Numerical study of stress distribution in sheared granular material in two dimensions. Phys Rev E 62(3):3882–3890. https://doi.org/10.1103/PhysRevE.62.3882
25. Bardenhagen SG, Guilkey J, Roessig KM, Brackbill JU, Witzel WM, Foster JC (2001) An improved contact algorithm for the material point method and application to stress propagation in granular material. Comput Model Eng Sci 2(4):509–522
26. Tran QA, Sołowski W (2019) Generalized interpolation material point method modelling of large deformation problems including strain-rate effects—application to penetration and progressive failure problems. Comput Geotech 106:249–265. https://doi.org/10.1016/j.compgeo.2018.10.020
27. Zhang DZ, Ma X, Giguere PT (2011) Material point method enhanced by modified gradient of shape function. J Comput Phys 230(16):6379–6398. https://doi.org/10.1016/j.jcp.2011.04.032
28. Bardenhagen SG, Kober EM (2004) The generalized interpolation material point method. Comput Model Eng Sci 5(60):477–496
29. Wallstedt PC, Guilkey JE (2008) An evaluation of explicit time integration schemes for use with the generalized interpolation material point method. J Comput Phys 227(22):9628–9642. https://doi.org/10.1016/j.jcp.2008.07.019
30. Sadeghirad A, Brannon RM, Burghardt J (2011) A convected particle domain interpolation technique to extend applicability of the material point method for problems involving massive deformations. Int J Numer Methods Eng 86(12):1435–1456. https://doi.org/10.1002/nme.3110
31. Homel MA, Herbold EB (2017) Field-gradient partitioning for fracture and frictional contact in the material point method. Int J Numer Methods Eng 109(7):1013–1044. https://doi.org/10.1002/nme.5317
32. Moutsanidis G, Kamensky D, Zhang DZ, Bazilevs Y, Long CC (2019) Modeling strong discontinuities in the material point method using a single velocity field. Comput Methods Appl Mech Eng 345:584–601. https://doi.org/10.1016/j.cma.2018.11.005
33. Nairn JA (2007) Numerical implementation of imperfect interfaces. Comput Mater Sci 40(4):525–536. https://doi.org/10.1016/j.commatsci.2007.02.010
34. Lemiale V, Nairn J, Hurmane A (2010) Material point method simulation of equal channel angular pressing involving large plastic strain and contact through sharp corners. CMES 70(1):41
35. Xiao-Fei P, Ai-Guo X, Guang-Cai Z, Ping Z, Jian-Shi Z, Shang M, Xiong Z (2008) Three-dimensional multi-mesh material point method for solving collision problems. Commun Theor Phys 49(5):1129. https://doi.org/10.1088/0253-6102/49/5/09
36. Nguyen VP, de Vaucorbeil A, Bordas S (2023) The material point method. Springer International Publishing, Cham
37. Barclay PL, Waters J, Zhang DZ (2023) Large deformation and brittle failure calculated using the dual-domain material point method. Comput Part Mech 11:169–183
38. Timoshenko SP, Gere JM (1961) Theory of elastic stability. Courier Corporation
39. Aristizabal-Ochoa JD (2013) Stability of imperfect slender columns with non-linear connections. Int J Non Linear Mech 54:66–75. https://doi.org/10.1016/j.ijnonlinmec.2013.03.015
40. Aristizabal-Ochoa JD (2013) Stability of multi-column systems with initial imperfections and non-linear connections. Int J Non Linear Mech 57:75–89. https://doi.org/10.1016/j.ijnonlinmec.2013.06.012
41. Aristizabal-Ochoa JD (2015) Stability of imperfect columns with nonlinear connections under eccentric axial loads including shear effects. Int J Mech Sci 90:61–76. https://doi.org/10.1016/j.ijmecsci.2014.11.005
42. Saffarini M, Sewell T, Su Y, Chen Z (2023) Atomistic study of the impact response of bicontinuous nanoporous gold as a protection medium: effect of porous-nonporous interface on failure evolution. Comput Mater Sci 228:112363